RESEARCH ARTICLE

ESPL WILEY

Decadal coastal evolution spanning the 2010 Maule earthquake at Isla Santa Maria, Chile: Framing Darwin's accounts of uplift over a seismic cycle

Diego Aedo[1,2,3] | Marco Cisternas[2,3] | Daniel Melnick[2,4] | César Esparza[5,6] |
Patricio Winckler[5,7,8] | Bladimir Saldaña[1,2,3]

[1]Departamento Ciencias de la Tierra, Facultad de Ciencias Químicas, Universidad de Concepción, Concepción, Chile

[2]Millennium Nucleus The Seismic Cycle Along Subduction Zones CYCLO, Valdivia, Chile

[3]Instituto de Geografía, Pontificia Universidad Católica de Valparaíso, Valparaíso, Chile

[4]Instituto de Ciencias de la Tierra, TAQUACH, Universidad Austral de Chile, Valdivia, Chile

[5]Centro Nacional de Investigación para la Gestión Integrada de Desastres Naturales (CIGIDEN), Santiago, Chile

[6]Departamento de Ingeniería Hidráulica y Ambiental, Pontificia Universidad Católica de Chile, Santiago, Chile

[7]Escuela de Ingeniería Civil Oceánica, Universidad de Valparaíso, Valparaíso, Chile

[8]Centro de Observación Marino para Estudios de Riesgos del Ambiente Costero (COSTAR), Valparaíso, Chile

Correspondence
Daniel Melnick, Instituto de Ciencias de la Tierra, TAQUACH, Universidad Austral de Chile, Valdivia, Chile.
Email: daniel.melnick@uach.cl

Abstract

Charles Darwin and Robert FitzRoy documented coseismic coastal uplift associated with the great 1835 Chile earthquake ($M > 8.5$) at Isla Santa María. In 2010, another similar earthquake (Mw 8.8) uplifted the island, ending the seismic cycle. The 2-m uplift in 2010 caused major geomorphic and sedimentologic changes to the island's sandy beaches. Understanding the processes governing these changes requires pre- and post-earthquake measurements to differentiate the effects of abrupt coseismic uplift from seasonal, annual, and decadal-scale signals. Here, we combine spatial analysis of aerial imagery, field geophysics, wind and wave models to quantify geomorphic changes between 1941 and 2021 along the main beach. During the late interseismic phase (1941–2010), a ridge-runnel system was formed and then buried by a frontal dune. Because of uplift in 2010, the shoreline prograded ∼20 m, the uplifted berm was abandoned, and a new seaward berm was built. In the following decade, the abandoned berm was eroded by widening of the backshore as the shoreline and dune advanced seaward. Over the surveyed eight decades, the shoreline prograded continuously, increasing from <1 m/year to up to 3–5 m/year after the earthquake. We infer that these changes were caused by a sedimentary disequilibrium driven by variations in relative sea level, moving formerly passive sands from eroding cliffs and marine depths into the coastal sedimentary system, thus promoting long and cross-shore sediment transport and, utterly, accretion. Our results have implications for studying beach evolution along tectonically-active coasts associated with drastic changes in relative sea level.

KEYWORDS
Chile 2010 earthquake, coastal geomorphology, coastal uplift, earthquake geomorphology, long-term beach monitoring, shoreline evolution

1 | INTRODUCTION

Sandy beaches are dynamic environments driven by the interaction of coastal morphology, sediment transport processes and changes in relative sea level over a wide range of time scales. Seasonal, annual and decadal changes are due to wave climate and wind direction, while centennial to millennial changes is due to processes that modify the sediment budget conditions, such as relative sea-level changes, coastal erosion, littoral drift, onshore-offshore transport, and climate change (Davies, 1974; Ranasinghe, 2016). Low-regularity natural events can also cause major changes in the coastal zone morphology, such as the role of extreme oceanographic forcing (Barnard et al., 2017; Harley et al., 2017; Masselink et al., 2016), local storm erosion (e.g., Winckler et al., 2017) as well as tsunamis waves (e.g., Liew et al., 2010; Tappin et al., 2012; Vargas et al., 2011). The availability of robust long-term decadal data and the use of novel techniques to characterize these processes are essential for understanding coastal response.

Sudden coseismic uplift and subsidence during great earthquakes have produced dramatic coastal changes (e.g., Meilianda et al., 2010; Plafker, 1972; Plafker & Savage, 1970; Vargas et al., 2011). The first accounts of sudden coastal coseismic uplift were made by Maria Graham following the 1822 Quintero earthquake in central Chile (Kölbl-Ebert, 1999), and by Robert FitzRoy and Charles Darwin after the 1835 Concepción earthquake in south-central Chile. FitzRoy and Darwin quantified coastal uplift at six sites surrounding the Arauco and Talcahuano Bays by leveling the elevation of dead mussels still attached to the emerged rocky shore (FitzRoy, 1839); following their footsteps, Melnick, Cisternas, et al. (2012) also used mussels to quantify coastal uplift in the same region during the 2010 earthquake. At Isla Santa María, FitzRoy and Darwin measured uplift of 2.4, 2.7 and 3.0 m at three sites located in the southern, central, and northern parts of the island, respectively. The observations of metric-scale uplift following the 1835 earthquake laid the foundation of Darwin's tectonic theories relating seismicity to the rise of mountain belts (Darwin, 1846; Wesson, 2017). In addition, FitzRoy and the officers of the HMS Beagle surveyed the topography of Isla Santa Maria and bathymetry of its surroundings producing a map that was used by Wesson et al. (2015) to quantify vertical deformation through the complete 1835–2010 seismic cycle.

Rapid coastal changes after coseismic subsidence were observed after the 2010 Chile (Martínez et al., 2015, 2021), 2011 Tohoku (e.g., Tappin et al., 2012) and 2004 Sumatra-Andaman (e.g., Choowong et al., 2009; Liew et al., 2010; Monecke et al., 2015, 2017) great earthquakes. These studies showed that, after coseismic subsidence, the shoreline typically receded by tens to hundreds of metres. Afterward, the beach may rapidly recover in the subsequent years and even grow back to its original position in some cases (Choowong et al., 2009). In the case of uplift, the beach prograde immediately; however, only a few studies have focused on monitoring this response. Some examples, mostly short-term monitoring, were reported after the 2004 Sumatra-Andaman (Rajendran et al., 2007), 2010 Chile (Jaramillo et al., 2012; Martínez et al., 2015) and 2016 New Zealand (Dickson et al., 2022; MacDonald et al., 2021).

Over several earthquake cycles, seismically modified coastal morphologies have been preserved. For example, Goff & Sugawara (2014) suggested a shaking-driven origin of beach ridges morphologies in eastern Japan by a series of immediate and delayed after-effects created by a cascade of geomorphological processes. Buried scarps were correlated with coseismic subsidence at Cascadia's Columbia littoral cell (Meyers et al., 1996; Peterson et al., 2010), Avachinsky Bay (Pinegina et al., 2020) and Chile (Cisternas et al., 2017). In Aceh, Indonesia's coast, Monecke et al. (2015) described the build-up of a high-elevation ridge in response to coseismic subsidence after the 2004 Sumatra-Andaman earthquake. In contrast, stair-step beach ridges stranded by coseismic uplift have been inferred in New Zealand (McSaveney et al., 2006), Chile (Bookhagen et al., 2006) and Kamchatka Peninsula (Pinegina et al., 2013). However, limited modern analogies are available to show how deformation caused by the seismic cycle drives the construction of beach ridge morphologies. This is especially so in places where uplift occurs.

Long-term coastal monitoring over decades spanning a great earthquake, would help to understand how their associated sudden land-level changes affect beach dynamics and morphology. Satellite and old aerial imagery provide a useful resource to assess long-term coastal changes based on high-resolution shoreline position measurements (Luijendijk et al., 2018; Mentaschi et al., 2018; Vos, Harley, et al., 2019; Vos, Splinter, et al., 2019). The use of unmanned aerial systems (drones) and the modelling of digital data have been useful to assess changes in sand volume and beach morphology (Casella et al., 2020; Gonçalves & Henriques, 2015; Pucino et al., 2021). Here, we combined aerial and spatial imagery analysis with topographic data, geophysical field surveys, with wind and wave models to study the shoreline evolution at Isla Santa Maria between 1941 and 2020 spanning the 2010 Maule earthquake (*Mw* 8.8). We integrated our results with interpretations of a paleoseismic study made at the island (Bookhagen et al., 2006).

2 | STUDY AREA

Isla Santa María (37°S; 73.5°W; ISM) is located 75 km landward of the Chile trench (Figure 1a,b) and 15 km above the interplate seismogenic zone juxtaposing the Nazca and South American plates (Melnick, Cisternas, et al., 2012). The geology includes a well-lithified Eocene-Miocene sedimentary bed-rock unconformably overlaid by poorly-consolidated marine and continental Pleistocene and Holocene deposits (Melnick et al., 2006). Geomorphologically, ISM may be divided into two units: a tilted upper surface of 40 to 80 m high and a Holocene sandy plain at elevations below 10 m (Figure 1c,d). This plain includes active dunes, wetlands, and a sequence of parallel beach ridges that have been attributed to coseismic uplift during multiple megathrust earthquakes (Bookhagen et al., 2006; Melnick et al., 2006). Net uplift of the island has been explained mainly by tectonic processes because the post-glacial isostatic rebound at its latitude is limited to the Main Cordillera, located 200 km west of the island. (Melnick et al., 2006; Rabassa & Clapperton, 1990).

During the 2010 earthquake, ISM was uplifted between 1.6 ± 0.1 and 2.2 ± 0.2 m. This range was estimated soon after the earthquake from measurements of uplifted intertidal mussels, campaign GPS observations, and resurveying a geodetic benchmark (Figure 1c; Melnick, Cisternas, et al., 2012; Melnick, Moreno, et al., 2012). During the 10 years that followed the Maule earthquake, the continuous GPS station STAM recorded 35 cm of subsidence; between 2010 and 2012 at ~50 mm/year with a decreasing logarithmic trend followed by a linear trend at 25 mm/year (inset in Figure 1c). The 2010 earthquake was preceded by the 1835 earthquake (*M* > 8.5), which uplifted the island 2.4 to 3 m (Darwin, 1839; King, 1839; Wesson et al., 2015). Using these reports and historical nautical charts Wesson et al. (2015) estimated that between the 1835 and 2010 earthquakes, the island subsided about 1.6 m at a rate of 11.3 ± 4 mm/year. The authors attributed this subsidence to interseismic locking and proposed that 0.15 to 0.3 m of the 1835 coseismic uplift was preserved as a crustal permanent deformation. This permanent deformation, saving ~10%–20% of coseismic uplift should be sufficient to explain the island's uplift rate of ~1.5 mm/year during the Holocene (Bookhagen et al., 2006) and Pleistocene (Jara-Muñoz & Melnick, 2015). To monitor the effects generated by these level changes on the island's coast, we studied all the island's sandy beaches, focusing on beach Tres Cuevas (TCUE), which is the largest and borders the beach ridge plain (Figure 1).

3 | MATERIAL AND METHODS

3.1 | Wind and wave data

Wind climate was characterized using readily available modelled data from the Climate Forecast System Reanalysis (CFSR) for the period 1985–2018 (Saha et al., 2010). CFSR hourly offshore surface winds at a node located 150 km westward from ISM were compared against local measured surface winds (2013–2015 monthly means) provided by Consorcio Eólico S. A (https://eolico.cl), showing good agreement.

From CFSR data, a wind rose was built and used to quantitatively describe the wind regime in TCUE.

Wave climate in TCUE was modelled herein using a combination of a Pacific-wide model implemented in WAVEWATCH III (Tolman et al., 2014) and the nearshore transformation model STWAVE (Smith, 2001); methodological details are included in the Supplementary Material. From the combination of both models, statistics of wave height and direction characterizing offshore wave conditions and a nearshore node located immediately off the coast of TCUE site were generated. Figure 1 presents the modal wave patterns expressed in
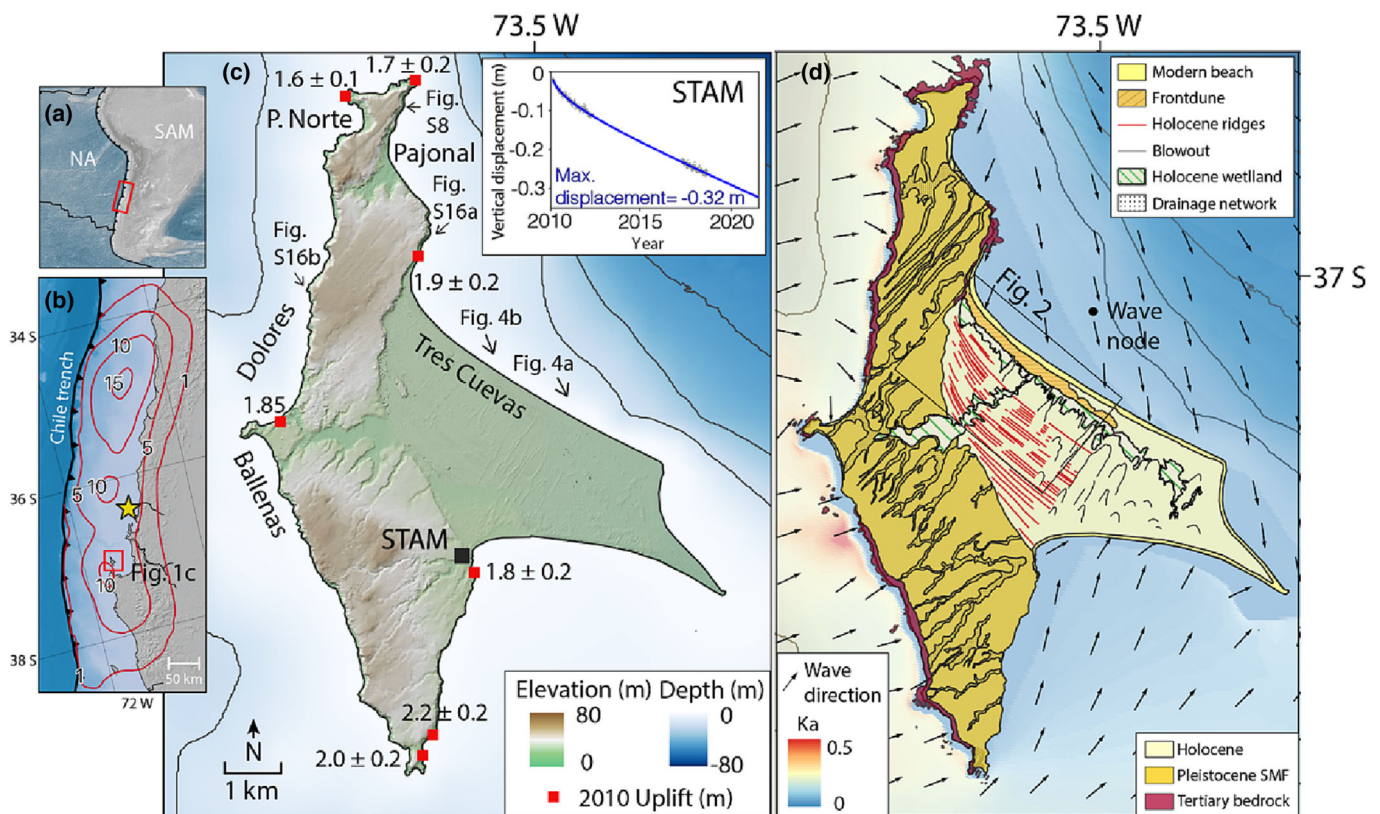
FIGURE 1 (a) Tectonic setting of the Nazca (NA)–South America (SAM) margin. (b) Location of Isla Santa María along the coast of Central Chile. Yellow star shows the epicenter of the 2010 Maule earthquake; 5-m coseismic slip contours in metres (Moreno et al., 2012). (c) Shaded relief digital elevation model (5-m resolution, derived from photogrammetric restitution of aerial photos) and bathymetry (20-m resolution from Jara-Muñoz et al., 2017). Coseismic uplift estimates are indicated by red squares (Melnick, Moreno, et al., 2012). Inset shows vertical displacement time series at continuous GPS site STAM (installed after the 2010 earthquake). Grey dots show daily positions and the blue line linear trajectory model Bevis & Brown, 2014; Melnick et al., 2017 with an estimated total amount of subsidence between 2010 and 2021. (d) Geologic and geomorphic map of Isla Santa María (modified from Melnick et al., 2006) with prevailing wave direction and agitation coefficient (Ka).

TABLE 1 Spatial imagery used in this work with estimated uncertainties. RMSE: root-mean-square error.

Images (sensor)	Collection	Date of acquisition (yyyy/mm)	Number of images	Resolution (m)	Geoaccuracy (m)	Runup (m)	RMSE (m)
Landsat 5 (TM)	LANDSAT/LT05/C01/T1_TO	1985/03–2011/04	103	30	7.03	2.77	10.68
Landsat 7 (ETM)	DSAT/LE07/C01/T1_RT_TO	1999/09–2021/02	242	15	6.95	2.77	10.58
Landsat 8 (OLI)	LANDSAT/LC08/C01/T1_RT_TOA	2013/03–2021/04	121	15	6.26	2.77	9.68
Sentinel 2A/2B (MSI)	COPERNICUS/S2	2015/09–2021/04	373	10	1.00	2.77	4.16
Air photos	IGM/SAF/Drone	1941/01–2021/03	18	0.25–1.69	3.67	2.77	6.50

terms of an agitation coefficient (Ka) defined as the ratio between nearshore and offshore wave heights (Ka > 1 represents an amplification and Ka < 1 a reduction). Figure S1 additionally includes wave roses offshore and at the nearshore node, as obtained from the time series included in Figure S2.

3.2 | Field and GPR surveys

GPR data were collected using a MALA Pro-Ex system with a 250-MHz shielded antenna and a GSSI UtilityScan system with a 350-MHz antenna at a sampling interval of 0.02–0.03 m. Topography for GPR transect was surveyed using a Trimble R8S differential GPS, synchronized during data acquisition to the STAM reference station (location in Figure 1c); locally we used interpolated heights from drone digital elevation data. GPR processing was completed with the GSSI RADAN 7 software and Matlab® package MatGPR R3.1 (Tzanis, 2010). We followed a standard processing routine with default settings which include desaturation (dewow), time zero correction, horizontal background removal, gain functions, bandpass filtering, and topography correction. The data visualization was supported by different excavations to calibrate and compare the signals with the sediments.

## 3.3 | Spatial imagery and shoreline change time series

Eighteen georeferenced aerial photos and 1169 orthorectified satellite images covering from 1941 to 2021 were used to quantify horizontal shoreline change (Table 1). The publicly available optical satellite data was extracted using the Python toolkit CoastSat (Vos, Splinter, et al., 2019). Landsat 5, 7 and 8 and Sentinel-2 images were pre-processed to remove cloudy pixels and enhance spatial resolution, then we removed duplicates and images with inaccurate geo-referencing (threshold at 10 m) to result in 839 images that were analysed. Using the CoastSat algorithm, the images were classified into four classes (sand, water, white water and others), and then the sand/water boundary was extracted using the Modified Normalized Difference Water Index (MNDWI). As the satellite imagery record

starts in the 1980s, we extended the time sequence backward by using older georeferenced aerial photos (shorelines position in Figure S3). We digitized the wet/dry line, which is assumed to be a good approximation of the high-water line (Monecke et al., 2015; Moore, 2000; Pajak & Leatherman, 2002). Shoreline positions were referenced to the last image collected days before the 27 February 2010 earthquake. Perpendicular transects crossing the shorelines were digitalized with a horizontal interval of 50 m (Figure 2). The horizontal change in the shoreline position was quantified by fitting a least-squares regression line to all shoreline points for each transect using Digital Analysis System 4.4 (DSAS), an extension of Esri's ArcGIS software (Thieler et al., 2009). Along each transect, the distance between subsequent shorelines was calculated and median and inter-quartile ranges were used as representative values. To measure changes in the width of the dune system, we visually traced the dune foot line from every image. This line was assumed to represent the most seaward limit of the dune, defined morphologically as an abrupt topographic change in the base of the dune (Sallenger, 2000). The rate of change was calculated using the same methodology as for the shorelines. The backshore width was represented in this study as the distance between the shoreline and the foot of the dune for each year.

A tidal correction was applied using water levels calculated with the global tidal model TPXO8-atlas (Egbert & Erofeeva, 2002) and a beach face slope of $m = 0.08$ (tidal range ~1.8 m) estimated from field measurements and digital elevation model (DEM) calculation (Figure S4) to relate each shoreline was translated to a reference elevation above mean sea level as follows:

$$\Delta x = \frac{z_{ref} - z_{wl}}{m}$$

where Δx is the cross-shore horizontal shift along the shore-normal transects, z_{ref} is the reference elevation, z_{wl} is the local water level at the time of image acquisition and m is the characteristic beach face slope. The horizontal positioning error of each shoreline was calculated as a result of the georeferencing offset and the shoreline variation due to wave run-up R (maximum elevation of shoreline oscillations caused by waves) calculated from modelled wave data using the relationship of Stockdon et al. (2006), Table 1. Georeferencing was cross-checked by comparing the position of stable and
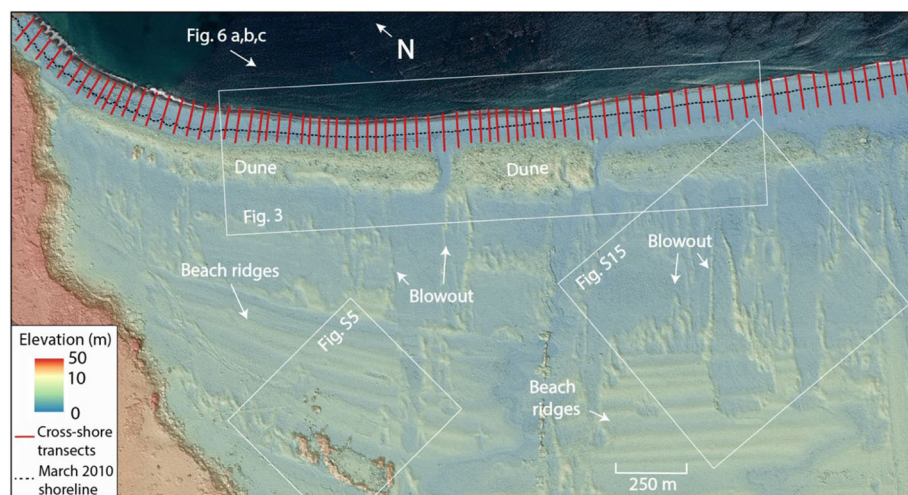
FIGURE 2 Topography of Isla María Coastal Plain (30-cm resolution, derived from photogrammetric restitution of 2016 drone photos) with all transects used and the 02/2010 shoreline as reference. Note the ridges sequence and the high topography of the frontal dune.

conspicuous ground control points (GCPs) in all images, including a landing strip, buildings, and fences, among others. All points were within less than 7.03 m of each other. The largest error was the variable run-up (average $R = 0.25$ m) leading to an error of 2.77 m in the horizontal shoreline position. The sum of geoaccuracy and run-up errors (root-mean-square, RMS) of individual shoreline positions is less than 10.68 m (Table 1). This value, which is within the expected error in shoreline detection, is mainly controlled by the effect of wave runup on the water level. It usually causes large horizontal translation of the waterline and shoreline position (Vos, Harley, et al., 2019; Vos, Splinter, et al., 2019).

The shoreline position was modelled at 5 sites using a linear trajectory method based on Bevis & Brown (2014) and Melnick et al. (2017) to model $x(t)$, the shoreline position time series along a coast-normal profile as follows:

$$x(t) = A(t - t_R) + B(t - t_{eq}) + C\sin\left(\frac{2\pi}{\tau}t\right) + D\cos\left(\frac{2\pi}{\tau}t\right)$$
$$+ E\log(1 + \Delta t - t_{eq}/T)$$

where A is the coefficient of a linear function, t_R is a reference time here defined as t_0, the start of the time series, B is the coefficient of a Heaviside jump to simulate a static coseismic offset during the 2010 Maule earthquake (t_{eq}), C and D are the coefficients of a truncated Fourier Series to account for seasonal variations (we used $\tau = 1$ year for annual periods), and E is the coefficient of the transient post-seismic logarithmic component. We define $\Delta t = 0$ for $t < t_{eq}$, and otherwise $\Delta t = t - t_{eq}$. T is a constant determining the timescale of the logarithmic transient. We used a value of $T = 0.1$ based on the study of Melnick et al. (2017) using GNSS data after the 2010 earthquake. We used the Matlab® function *lscov* to perform the least-squares inversion in the presence of covariance accounting for the shoreline positioning uncertainties.

3.4 | Photogrammetric reconstruction and DEM analysis

Aerial photos from March 2010 (1:20 000, collected by Servicio Aerogotogramétrico; SAF), and Mavic 2 Pro Drone flights conducted over the study area (Figure 2) in February 2016 and March 2021 were used. Photos were processed with Agisoft Metashape to obtain orthophoto mosaics and DEMs. The quality assessment was conducted by positioning seven GCPs using a Trimble RTK dGPS mounted on a pole (Figure S5). The dGPS was also mounted on a backpack to acquire continuous points at a frequency of 1 Hz collecting 421 independent control points (ICPs). The points surveyed referred to the time series of the STAM continuous GPS base station (Figure 1c). This approach was also used in an additional area of the beach to double-check the 2021 elevation model (with 6 GCPs and 547 ICPs; Figure S5). Matlab® scripts modified from Casella et al. (2020) were used to compare the ICPs elevation values with the DEMs at the same points to estimate the models' quality.

Elevation changes were calculated based on DEMs of Difference (DoDs) and we considered the error of each DEM to calculate limit of detection thresholds for each DoD using the open-source Python

package Sandpyper (Pucino et al., 2021). These thresholds were calculated as the subtraction of the different DEMs over a shared area (same location used to estimate the model quality) and were defined as the expected error in the DoD inherent to DEM noise (Figure S6). We evaluated the statistical distribution of error values, and a series of statistical parameters were calculated (Table S1). The normalized median absolute deviation was used due to the non-normality of the data (Wang et al., 2015). Finally, because the models were levelled referenced to the island's position in 2021, the elevation of the 2010 and 2016 DEMs was corrected to their corresponding level by adding 0.29 and 0.10 m, respectively, to account for the subsidence estimated from the STAM station trajectory model (inset of Figure 1c). Geomorphological and volumetric changes were evaluated for the 2016–2010, 2021–2016 and 2021–2010 time periods.

4 | RESULTS

4.1 | Decadal changes in coastal landforms

The 1941 photo, the oldest available for TCUE beach, showed a shoreline parallel, narrow, and elongated trough, on the intertidal zone (Figure 3a). The zone between the trough and the surf exhibited a parallel, emerged ridge. In the central part of the studied beach, a rip channel cut through the ridge discharging the water trapped in the trough into the sea. Because the ridge and trough fit the classical description of 'ridge and runnel beach' proposed by King & Williams (1949), we will henceforth use this term to refer to this feature. Likely, high waves during high tide overtop the ridge and flood the runnel, as evidenced by the wet sand shown in the photo (Figure S7). Landward of the runnel and far from the influence of the waves, a narrow longitudinal eolian accumulation of sand is observed, including blowouts oriented to the island's predominant winds (Figure S1). The longitudinal accumulation is not developed enough to form a frontal dune (Figures 3a and S7).

Between 1941 and 1 week before the 2010 earthquake the shoreline, and its frontal beach berm, advanced. Significantly, the ridge and runnel were buried by eolian sand that formed a wide frontal dune (Figure 3b). The abrupt 2010 coseismic uplift caused the abandonment of the beach berm. Soon after, this uplifted berm was eroded and a new beach profile was formed, as seen in the inset of Figure 4a. The most remarkable post-uplift change was the rapid advance of the beach. A very wide backshore resulted from the deposition of a large amount of sand (Figure 4b). This large sediment mobilization is also observed in other areas of the island where uplifted rocky platforms have been completely covered by sand and transformed into new beaches (Figure S8).

4.2 | Ground penetrating radar images

Post-2010 profiles across the beach showed different behaviours alongshore (Figure 3d,e). While the northernmost part of the beach exhibited a short backshore (<100 m) and a high frontal dune (>6 m), the southern part showed a wider backshore (>150 m) and a smaller dune (3–4 m). In agreement with the evolution inferred from imagery
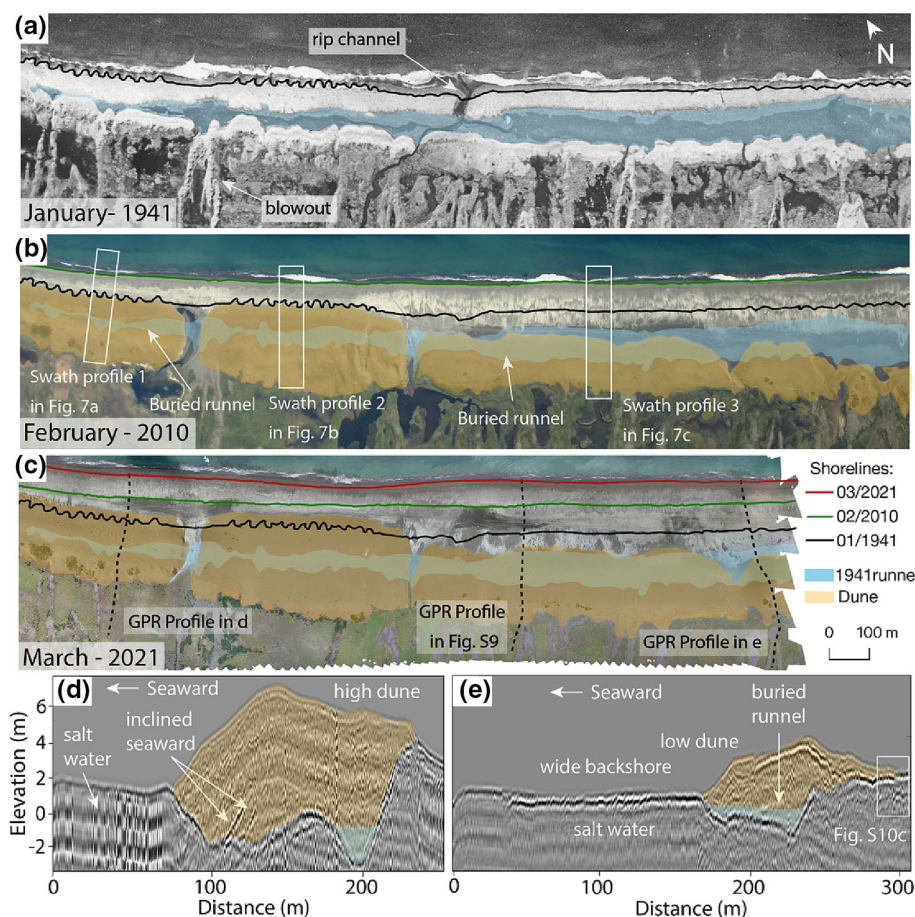
FIGURE 3 Vertical air photos from 1944, 2010, and 2021 (sources: IGM, SAF and drone flight by D. Aedo) showing geomorphic changes at Tres Cuevas beach. (a) Decades before the earthquake (Tide: −0.4 m); (b) 1 week before the earthquake (Tide: 0.3 m); and (c) 11 years after the coseismic uplift during the 2010 earthquake (Tide: −0.2 m). Note differences in sandy beach width and the burial of the 1941 morphologies by the growth of the frontal dune. An uninterpreted version of these photos is in Figure S7. (d,e) GPR beach profiles showing the difference in backshore width along the beach, dune elevation, progradation signals and buried sediments.

(Figure 3a–c), GPR profiles were able to recognize the dune-buried ridge and runnel system observed in the 1941 photo (Figures 3d,e and S9). Field excavations revealed the GPR signals to represent dark beach sand with high content of heavy minerals under a layer of marine shells and eolian sediment burying them (Figure S10a–d). Excavations on the backshore of the modern shoreline showed the same black and shelly sand as seaward, 6°-sloping layers (Figure S10e), similar to the slope at the active shoreface, which ranges between 6° and 9°.

4.3 | Time-series analysis revealing TCUE shoreline migration

Figure 5 summarizes the pre- and post-earthquake rates of shoreline changes on studied beaches inferred from 1941 to 2021 imagery, as well as the TCUE time series of horizontal coastline position. Before 2010 uplift, TCUE prograded at an average low rate of 0.6 m/year (Figure 5a). Following the earthquake, the accretion rate in TCUE accelerated to an average of 3.4 m/year. (Figure 5b). Although these rates in cross-shore transects (Figure S11a,b) showed no clear trend before 2010, in post-earthquake time they exhibited an accelerated progradation, from 3 to 5 m/year, in the northern transects, and a slower rate between 1.5 and 3 m/year, in the south (Figure S11e).

TCUE is sheltered to the predominant swells which (Figure S1), as a consequence of wave refraction and diffraction in the northern part of the island, have significant wave heights below 1.5 m near the surf zone (Figure S2), values that are much smaller than the offshore wave heights. The 2010 uplift did not significantly affect these parameters at the beach (<0.02 m). The trajectory model of TCUE shoreline position since 2000 reproduced well the summer/winter interseasonal variation of the beach position as well as the slow secular coastal progradation before coseismic uplift (Figure 5c). Immediately after the earthquake, the model accounted for a sudden beach advance of 18 ± 10 m, followed by a steady progradation at a higher pace that gradually decreased over the following decade. The complete time series since 1941 is shown in the inset of Figure 5c. A comparison of summer images at TCUE revealed a mean shoreline advance of 51 ± 13 m between 1941 and 2010. After that, until 2021, the coast advanced 63 ± 7 m on average. Thus, the TCUE shoreline progradation was larger in the decade after the earthquake than in the seven decades before.

The monitoring of the dune toe showed seaward advancement both before and after the 2010 uplift (Figure S11c,d). The prior sequence showed a low rate of advance at an average of 0.7 m/year, except in the beach middle, where the rate was between 1.2 and 1.8 m/year. After the coseismic uplift, the dune front advanced rapidly at an average rate of 2.8 m/year, similar to even larger than the rate of shoreline advance itself. In northern and middle parts of the beach, maximum rates of about 3–4 m/year were reached (Figure S11f). In comparison, the TCUE backshore was narrower in the years before the 2010 uplift (<50 m in 2007). Between 2014 and 2019 the extension of the backshore ranged between 57 and 78 m. As total, between 2010 and 2021 the backshore prograded more than 50 m (Figure S11f).

FIGURE 4 Oblique aerial photos showing changes in the shoreline associated with coseismic uplift in 2010. (a) 13 days after the earthquake (Tide: −0.4 m) and (b) 11 years after the earthquake (Tide: −0.2 m).
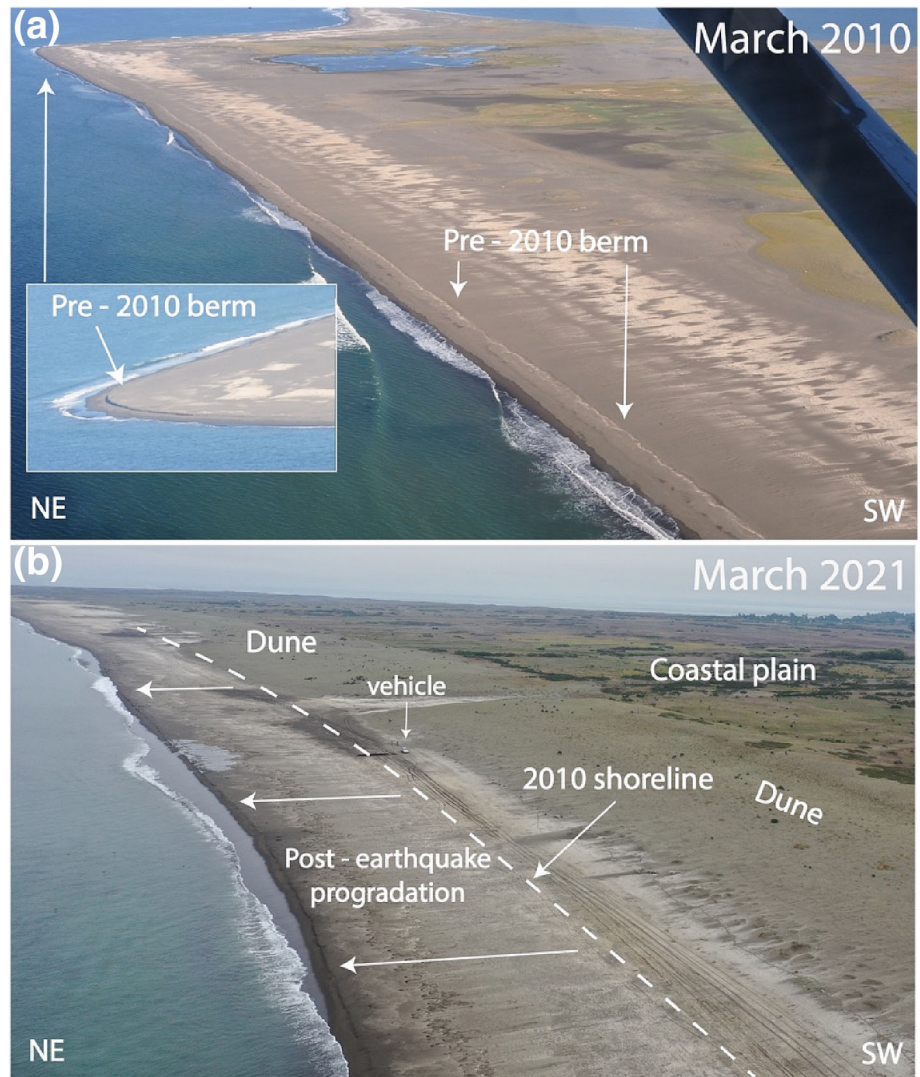

4.4 | Time-series analysis at other beaches

Before 2010 uplift, the E-facing Pajonal beach and WSW-facing Ballenas beach were relatively stable, while the WNW-facing Dolores beach receded at a rate lower than 1 m/year (Figure 5a). Puerto Norte, oriented to the W, prograded at rates lower than 1 m/year (Figure 5a). All beaches changed in the years following the 2010 uplift, showing eroding and prograding patterns on the western and eastern coasts, respectively. The beaches of Puerto Norte, Dolores, and Ballenas, which are exposed to predominant swells (Figure S1), receded at rates between 1 and 1.5 m/year, whereas sheltered Pajonal accreted at rates between 1.5 and 3 m/year, similar to TCUE. As on the main study site, all these beaches also showed interseasonal variation and an abrupt co-seismic advance with similar values of 14 ± 3 m for Puerto Norte, 17 ± 7 m for Pajonal, 22 ± 3 m for Dolores, and an exceptionally high advance of 75 ± 1 m for Ballenas (complete trajectory models are included in Figure S13).

4.5 | Topography

In general, our DEMs obtained from imagery in TCUE presented good resolution and low associated vertical RMSE errors. They ranged

between 56 cm for 2010 imagery and 21 cm for 2021 (full accuracy results in Figure S5). Oblique views of TCUE using the Digital Surface Models (Figure 6a–c) showed the same morphological features as the aerial photographs in Figure 4, including an uplifted and abandoned berm, a wide backshore zone, and a frontal dune at the back. LoD threshold values used to calculate the DoD ranged between 55 cm and 18 (Supplementary Table 1). The 2016–2010 DoD showed that almost the whole area suffered erosion between those years. The 2021–2016 DoD (Figure 6e) showed little change in the backshore, erosion in the dune back, and again sediment accretion on both the beach front and the dune backshore. Finally, the 2021–2010 DoD (Figure 6d) showed that erosion predominated in this period, focused on the backshore and at the dune back. There was a large accretion of sediments on the beachfront due to the advance of the shoreline and accumulation on the dune front. The measured values for the study area (Figure 6f) showed a total erosion volume of $1.2 \times 10^5 \pm 3.7 \times 10^4$ m^3 (296 ± 91 m^3/m) between 2021 and 2010.

Post-2010 evolution of the beach profiles showed marked erosion of the pre-earthquake berm (Figure 7). Balance of transported sand, between the years 2010, 2016 and 2021, is shown in the insets of Figure 7. In the total sum of sediment, the loss due to erosion is balanced by the accumulation of sand due to beach and dune progradation. In SP1, north of the beach, the sediment balance was
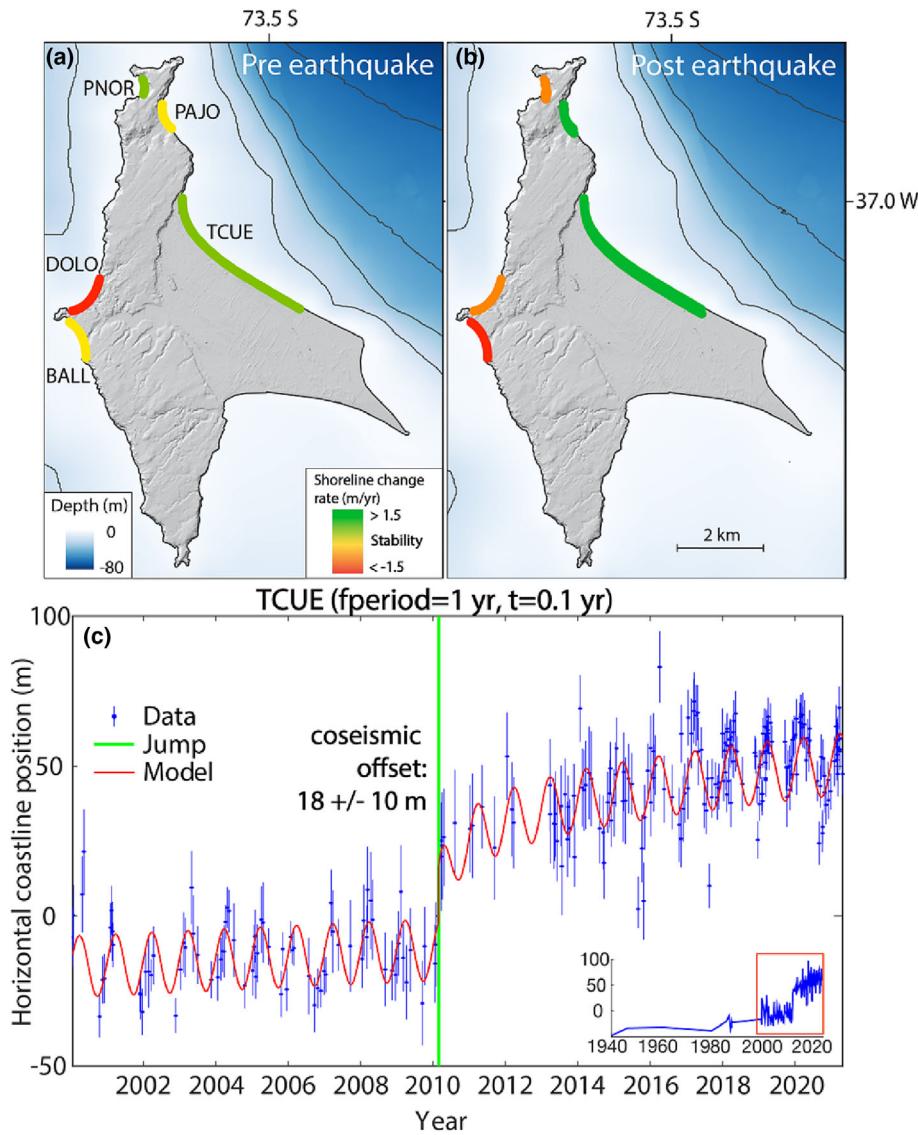
FIGURE 5 (a,b) Shoreline rate changes before and after the 2010 earthquake in the island beaches, classified according to categories defined by Martínez et al. (2021): high erosion in red (>1.5 m/year), stability in yellow (between −0.2 and +0.2 m/year) and high accretion in green (> +1.5 m/year). PNOR: Puerto Norte, DOLO: Dolores, BALL: Ballenas, PAJO: Pajonal. (c) Trajectory model of Tres Cuevas horizontal shoreline position change showing the 2010 earthquake abrupt advance, the progradation rate change and the stational variation. See methods section for details on the model. The shoreline position is referenced to the 2010 pre-earthquake (zero = 19/02/2010). Inset in the lower right shows the complete time series since 1941. Trajectory model of sites PNOR, PAJO, DOLO and BALL are shown in Figure S13.

positive after 11 years after the coseismic uplift. This was only observed in this profile because in SP2 and SP3, centre and south of the beach, the erosion between 2016 and 2010 was predominant and produced a total sediment loss balance between 2021 and 2010.

5 | DISCUSSION

A strong erosional trend has been observed in sandy beaches along the Chilean coast during the last four decades (Martínez et al., 2021). Changes in wave climate and relative mean sea level, a reduction in sediment supply from rivers, and local anthropogenic effects have been proposed to explain this widespread observation along nearly 2000 km of the tectonically-active Chilean coast. In contrast, TCUE beach and the coastal plain behind have prograded continuously during the late Holocene (Bookhagen et al., 2006; Melnick et al., 2006), as well as during the last eight decades under scrutiny. Its protection from predominant winds and waves (Figures 1d and S1), which combined enhance sediment accumulation, could explain this trend. TCUE even differs from the other beaches of the same island that follow a rather erosive trend (Figures 5 and S13).

5.1 | Pre-2010 beach progradation

The morphological changes experienced by TCUE during the seven decades before 2010 are represented in a conceptual model (Figure 8). The early interseismic phase shows a low dune probably because the aeolian sand supplied from the SW is not retained by the existing accommodation space and fast removal by coastal erosion processes (Figure 8a). In fact, the accommodation space during the interseismic phase was decreasing continuously as a result of relative sea-level rise induced by tectonic subsidence at 10 mm/year (Melnick, Moreno, et al., 2012; Wesson et al., 2015). The most significant change during the pre-earthquake phase at TCUE is the development of a large frontal dune that buried the former beach, including its conspicuous ridge and runnel system. As a consequence, the backshore zone narrowed dramatically, despite the beach accretion (Figures 8b, S11g and S14). Development of outsized dunes on coastal plains has been related to low progradation, which allows more time for higher topography construction (Bristow & Pucillo, 2006; Brooke et al., 2008). The pre-earthquake dune development at TCUE could respond to a positive balance of eolian sediment input from the southwest, which in turn would depend on other processes, including

FIGURE 6 (a–c) Digital surface models of the Tres Cuevas beach created using air photos for 2010 (SAF) and drone surveys for 2016 and 2021. (d–f) Digital elevation model (DEM) of difference showing the elevation changes after the 2010 earthquake. Inset in each figure shows the mobilized sand volume above mean sea level as estimated using pairs of digital elevation models. (f) The position of the GCP (ground control point) and ICP (independent control points) used to measure the topography accuracy (further details may be found in Figure S5). (d) Vertical difference in metres.
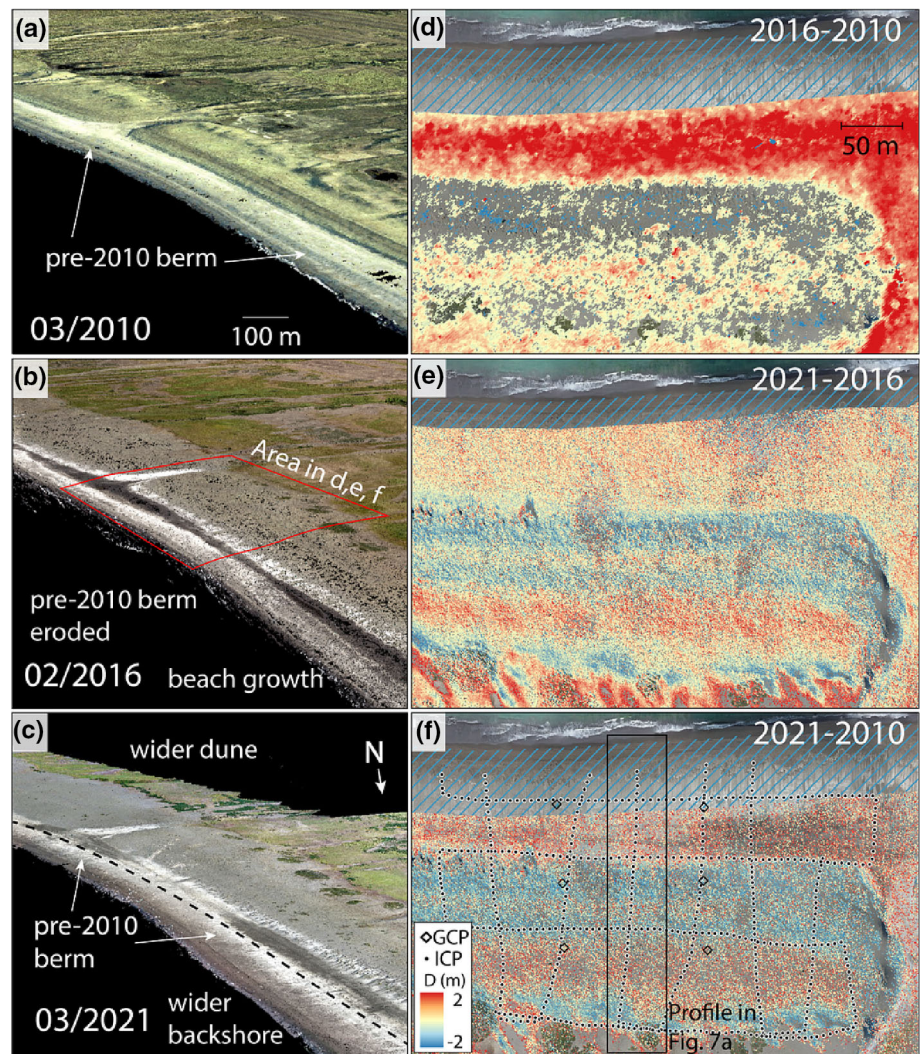
changes in relative sea level, waves and sudden sediment inputs triggered by earthquakes.

ISM experienced interseismic subsidence, at an average rate of 10 mm/year between 1835 and 2010, causing a fast relative sea-level rise (Wesson et al., 2015). Sea-level rise often leads to coastal erosion (Bruun, 1962), which eventually delivers significant volumes of sediment to the beach (Brooke et al., 2015; Hesp, 2013; Hesp et al., 2022). In South Australia, a new transgressive eolian sand sheet, and eventually a dune field, was a result of the high onshore sediment supply observed during the 2010s as a consequence of sea-level rise induced by climate change (Hesp et al., 2022). In another example, erosion induced by a 0.5–1.0 m coseismic subsidence during the 2004 Sumatra earthquake supplied sediment to build a particularly high beach ridge 2 years after the earthquake (Monecke et al., 2015). Because ISM experienced rather fast interseismic subsidence before the 2010 earthquake at 10 mm/year, sediments provided by coastal erosion from the surrounding cliffs and rock platforms resulted in burial of the ridge and runnel system that was exposed in the 1940s.

The dominant winds at ISM have produced conspicuous aeolian morphologies such as blowouts on the coastal plain (Figure S15). These features, which have been moving rapidly during the studied period, evidence important erosion on the plain and a northeastward transport of sediments towards the TCUE frontal dune. Although the offshore wave regime is characterized by predominant waves from the SW, local waves orthogonally arrive from the NW to TCUE as a consequence of refraction and diffraction on the northern tip of the island (Figure S1). A combination of (i) aeolian sand transport driven by the prevailing SW winds and (ii) longshore sediment transport from the slow erosion of the northwest cliff could explain the convergence of sand from both the land and sea at the TCUE beach (Figure 8a,b). These mechanisms characterizing the sheltered eastern portion of the island likely explain the extended plain backing TCUE, while the exposed western coast is characterized by steep cliffs and narrow pocket beaches (Figure 5).

A sudden supply of sediments to the ISM coast during the studied period was likely yielded by landslides triggered by the 21 May 1960 earthquake (*Mw* 8.1). No vertical deformation was reported at ISM by Plafker & Savage (1970) while Ojeda et al. (2020) suggest only a few centimetres uplift. This event occurred only ∼50 km south of ISM and generated landslides along the island's coastal cliffs according to eye-witnesses (similar to the 2010 earthquake; Melnick, Moreno, et al., 2012; Figure S16). Because the sediments composing the ISM cliffs have similar sedimentological characteristics to those of the modern TCUE beach and dune (Jara-Muñoz & Melnick, 2015), the 1960 landslides likely produced positive, although punctual, changes in the sedimentary budget of the TCUE beach. The predominant longshore currents (Figure S1) would favour the transport of
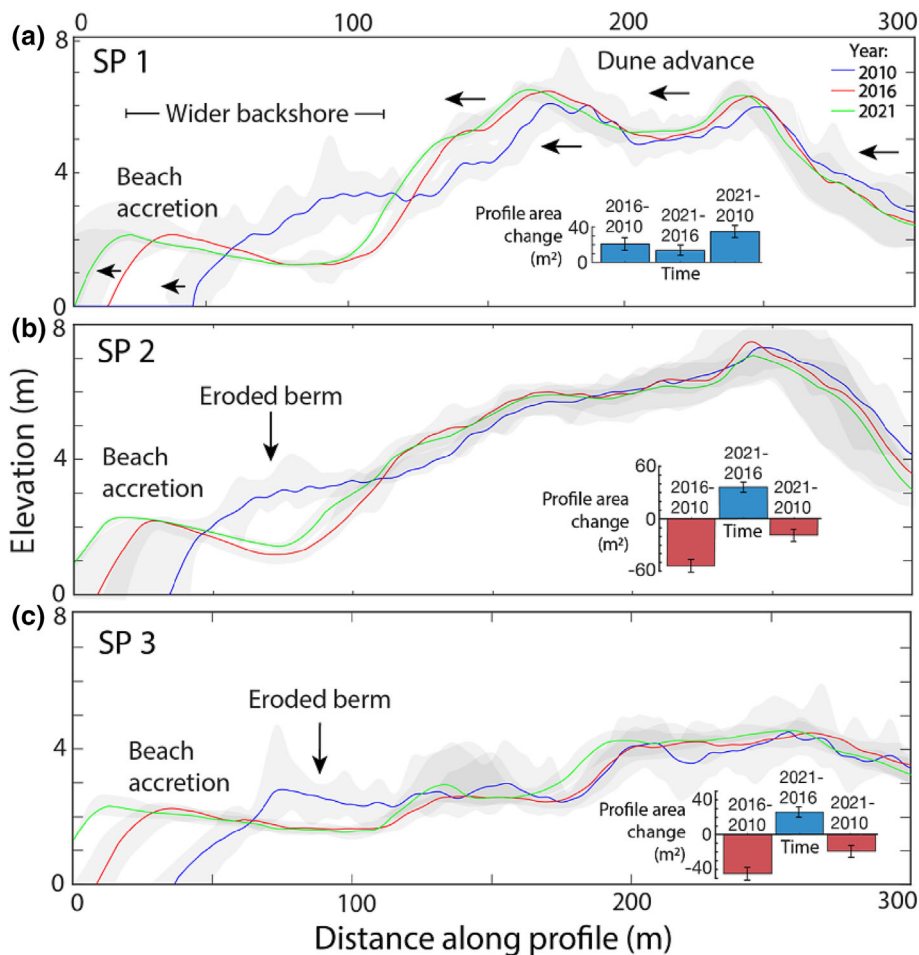
FIGURE 7 (a–c) Swath profiles (SP) of Tres Cuevas beach showing the morphological changes. Location of profiles in Figure 3b. Note erosion of the uplifted berm. Insets show bar plots of area change calculated by differencing the respective profiles; blue represents positive change (sand accumulation) and red negative change (erosion).

sediments from the eroded northwestern cliffs towards the TCUE plain (Figure S16a).
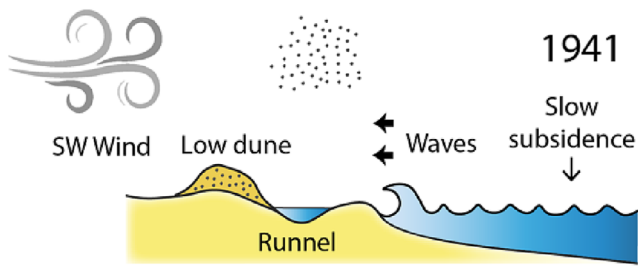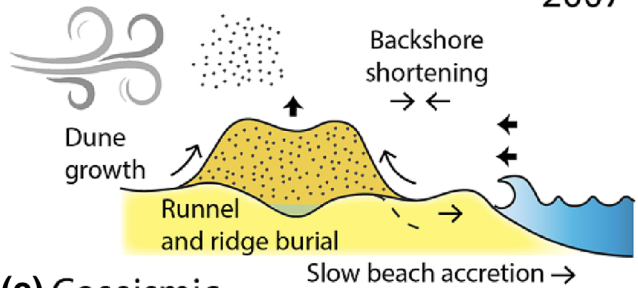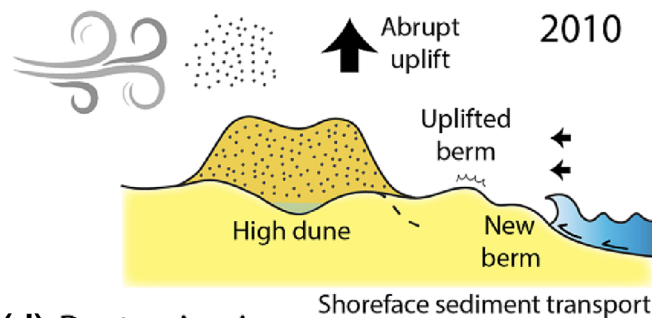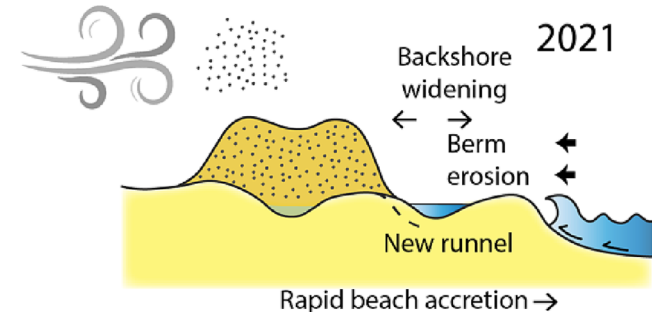
5.2 | Beach response to the 2010 uplift

The immediate consequence of the ∼2-m coseismic uplift at ISM was the widening of the TCUE beach, abandonment of its former berm, and construction of a new seaward berm (Figure 8c). Furthermore, there was an abrupt advance of the shoreline of all the studied beaches with values in the order of tens of metres (Figures 5b and S10). A particular case is Ballenas beach, which accreted by ∼75 m (Figure S13d) as a consequence of the uplift, after which it recovered the erosional trend before the 2010 earthquake. However, the new beach began to erode rapidly after 2010. The changes experienced by TCUE beach following 2010, including the erosion of the raised and abandoned berm, and the formation of a wide plain containing a new ridge and runnel system (Figure 8d), were probably the result of a positive sedimentary budget. This increase in available sediment has likely been controlled by RSL fall, rapid sediment mobilization and the sudden availability of new waterborne sediment inputs.

A sudden lowering of the relative sea level creates a shallower shore face which alters the equilibrium dune-beach-berm profile (i.e., disequilibrium overfit case) resulting in a sediment overload and cross-shore sand transport (Anthony & Aagaard, 2020). This process may in turn result in sediment accretion and shoreline progradation by the inverse mechanism proposed by Bruun (1962). Conversely, where

the relative sea level has risen due to coseismic subsidence, strong coastal erosion occurs (e.g., Peterson et al., 2000; Pinegina et al., 2020). At ISM, coseismic uplift had caused a shoreface disequilibrium that in turn triggered a rapid transport of sand to the beach (Figure 8c). This could explain the rapid accretion of sediments at TCUE, which is sheltered from the dominant winds and waves (Figure S8). Although tsunamis are another important process that mobilizes sediment for coastal changes (Monecke et al., 2015), neither the post-1960 and post-2010 earthquake images nor our field survey shortly after the 2010 event suggest a significant impact by both tsunamis at TCUE. The 2010 tsunami impacted mostly the western shores of ISM and generated only a minor swell along the eastern coastline, owing to more sheltered conditions. The effect of tsunamis along TCUE is therefore most likely minor compared to the sediment imbalance caused by coseismic uplift.

After the uplift in 2010, the TCUE beach sediments began to be vigorously mobilized. Between 2010 and 2016 a large volume of sand was eroded from the uplifted and abandoned pre-earthquake berm (Figure 6). Most of the resulting mobilized sediment probably contributed to the horizontal progradation of the beach although the volume balance between 2010 and 2021 was still negative (results in Section 4.5). The total volume of sand lost due to erosion of the uplifted beach and berm has not been yet recovered. This negative balance is evidenced in SP2 and SP3 (Figures 7b,c). SP1 (Figure 7a) shows a somewhat different behaviour in the northwestern part of the beach since, despite the initial erosion of the uplifted berm, beach accretion and dune advancement have resulted in a positive sand

(a) Interseismic

SW Wind Low dune Waves Slow subsidence Runnel 1941

(b) Late interseismic

Dune growth Runnel and ridge burial Backshore shortening Slow beach accretion → 2007

(c) Coseismic

High dune Abrupt uplift Uplifted berm New berm Shoreface sediment transport 2010

(d) Post-seismic

Backshore widening Berm erosion New runnel Rapid beach accretion → 2021

FIGURE 8 Schematic representation of the 8-decades chronology of the Tres Cuevas beach in Isla Santa Maria. The proposed coastal evolution shows a constant beach progradation accelerated by the 2010 coseismic uplift, the encounter between the prevailing wind and the waves arriving on the beach and a frontal dune that buries the coastal morphologies of decades before the earthquake.

balance. Possibly in this area, the dune advanced further due to the wind shadow resulting from the closer position of the cliff to the beach. Therefore, we propose that analogous processes as those inferred during relative sea-level rise (Brooke et al., 2015; Hesp, 2013; Hesp et al., 2022) have affected the beach during the decade after the 2010 earthquake as a result of 32 cm of land subsidence (Inset in Figure 1c), which fuelled the coastal system with a large volume of available sediment for beach accretion.

As proposed, landslides triggered by the 2010 shaking could have contributed significant amounts of sediment to the littoral system. Coastal accretion has been liked to seismic-driven mechanisms (e.g., strong ground motion causing landslides and, utterly, fluvial transport). For example, Moseley (1991) charted a new beach ridge on the arid Peruvian coast after the 1970 earthquake (Mw 7.7). The shaking triggered inland landslides that mobilized sediments into the catchments, which were then transported to the coast during the rainy season of the 1972–1973 El Niño event. Similar processes occurred at Sendai Plain in Japan, following the 2011 Tohoku earthquake and in New Zealand, as a consequence of Alpine fault activity (Wells & Goff, 2006; Goff & Sugawara, 2014).

The shaking of the 2010 earthquake produced large landslides in the coastal cliffs surrounding ISM (Melnick, Moreno, et al., 2012; Figure S16). Considering the proximity of some failed cliffs to the TCUE beach and the predominant longshore currents at the site (Figures 1d and S1), it is likely that the landslide sediments eventually became part of the sedimentary budget of the beach (Figure S16a). After the 2010 earthquake the progradation rates in the northwestern part of the beach -closer to the failed cliffs- were higher (Figure S11b). The proximity to the cliff, the direction of the currents, transporting sand towards the beach, as well as the shallower bathymetry making a disequilibrium, overfit likely mobilized sand towards the TCUE beach.

5.3 | Interpretation of beach ridge plains as records of past earthquake cycles

This study shows a net shoreline progradation at the TCUE beach during eight decades, which includes the uplift caused by the 2010 earthquake (Figure 5a,b). This persistent behaviour is remarkable, as it occurred during the relatively slow sinking process occurring in the late interseismic period and immediately after the rapid coseismic uplift. We herein hypothesize that this modern analog, and the similar coseismic uplift observed in the 1835 earthquake by Darwin and Fitzroy (Darwin, 1839; FitzRoy, 1839), could suggest that progradation has been persistent during previous seismic cycles, on the scale of thousands of years. Along this line, we propose that the abandoned beach ridges behind TCUE are a consequence of such cycles. Bookhagen et al. (2006) interpreted them as berms representing the last storms before sudden coseismic uplift associated with past large earthquakes. In this study, we show that construction of the ridge-swale topography is more complex and likely involves interseismic, coseismic and post-seismic stages. At a short scale, the coseismically uplifted berm was rapidly eroded in the subsequent years (Figures 6 and 7). Additionally, the intertidal ridge and runnel system, another potential candidate to explain the ridge-swale topography, was buried before the uplift. These findings at TCUE are inconsistent with the conceptual model of Bookhagen et al. (2006) because our observations suggest that the berm formed in the last storm before the earthquake would not be preserved in the millennial-scale geomorphological record. However, although we cannot discard that a new berm will form in the following decades, it will no longer represent a record of coseismic uplift but rather of the post- or interseismic stages without a clear temporal relation to the timing of the earthquake.

6 | CONCLUSIONS

We observed and quantified morphological changes along sandy beaches at ISM over eight decades spanning the 2010 Chile earthquake. We related the observed changes to the different phases of the seismic cycle, including interseismic subsidence, 2 m of coseismic uplift and subsequent post-seismic subsidence.

During the interseismic phase before the 2010 earthquake, the shoreline of the main studied TCUE beach prograded slowly and continuously at a rate below 1 m/year. At the same time, an intertidal ridge-runnel system was buried by the seaward advance of a large frontal dune. Both processes likely resulted from a combination of factors, including a gradual sediment supply yielded as a consequence of the interseismic subsidence at ∼10 mm/year, wind ablation and deposition, longshore and cross-shore sediment transport in the surf zone, and sudden sediment inputs from earthquake-triggered landslides.

Over the coseismic phase, the shoreline suddenly advanced seaward about 20 m as the beach was suddenly uplifted 2 m. Consequently, the pre-earthquake beach and berm were separated from the intertidal zone inland. Landslides in nearby cliffs triggered by seismic shaking during the 2010 earthquake likely supplied sediments to fuel the shoreline progradation. A new seaward beach and berm started to be built soon after the earthquake.

During the following post-seismic decade, the shoreline continued prograding at a faster rate greater than 1 m/year associated with an advance of the foredune, and widening of the backshore. Interestingly, this progradation has continued to occur despite experiencing very fast subsidence at a rate of ∼25 mm/year as shown by GPS, which is more than twice the rate before the earthquake. This process was caused by the availability of formerly passive marine sands which became available as a consequence of the coseismic uplift, of increased sediment supply from landslides triggered by the 2010 earthquake, and continuous aeolian input. Marine sediments were then transported by wave-driven longshore and cross-shore transport, modelled by variation in relative sea level.

Our results, based on the 2010 modern analog, suggest that the progradation of the Holocene plain of beach ridge-runnel pairs has occurred continuously and is not only associated with the coseismic uplift of previous earthquakes but also with interseismic and post-seismic changes in relative sea level. Therefore, the beach ridge records relative sea-level changes during complete seismic cycles including sudden coseismic uplift and slow interseismic subsidence, which balance the rate of plain progradation. This conclusion is useful to interpret the record of past earthquakes in Holocene beach-ridge plains, at ISM and other tectonically-active coasts.

AUTHOR CONTRIBUTIONS

DA, MC and DM led the preparation of the manuscript and conceptualized the research. DM and MC obtained the main source of funding for this project. DA, MC and DA performed the shoreline analysis and photogrammetric reconstruction. DM performed the trajectory model. CE and PW performed the wind data collection and wave modelling. DA, MC, DM and BS collected field data, GPR survey and assisted in logistics. MC and DM supervised and revised the initial manuscript. All authors contributed to the review and editing of the final manuscript.

DATA AVAILABILITY STATEMENT

The data presented in this paper are made available within the paper itself and the supporting information in graphical, table and text format. For more information, please contact the corresponding author.

ORCID

Diego Aedo https://orcid.org/0000-0002-7834-9523

REFERENCES

Anthony, E.J. & Aagaard, T. (2020) The lower shoreface: Morphodynamics and sediment connectivity with the upper shoreface and beach. *Earth-Science Reviews*, 210, 103334. Available from: https://doi.org/10.1016/j.earscirev.2020.103334

Barnard, P.L., Hoover, D., Hubbard, D.M., Snyder, A., Ludka, B.C., Allan, J., et al. (2017) Extreme oceanographic forcing and coastal response due to the 2015–2016 El Niño. *Nat Commun*, 8(1), 14365. Available from: https://doi.org/10.1038/ncomms14365

Bevis, M. & Brown, A. (2014) Trajectory models and reference frames for crustal motion geodesy. *Journal of Geodesy*, 88(3), 283–311. Available from: https://doi.org/10.1007/s00190-013-0685-5

Bookhagen, B., Echtler, H.P., Melnick, D., Strecker, M.R. & Spencer, J.Q.G. (2006) Using uplifted Holocene beach berms for paleoseismic analysis on the Santa María Island, south-Central Chile. *Geophys Res Lett*, 33(15), L15302. Available from: https://doi.org/10.1029/2006GL026734

Bristow, C.S. & Pucillo, K. (2006) Quantifying rates of coastal progradation from sediment volume using GPR and OSL: the Holocene fill of Guichen Bay, south-East South Australia. *Sedimentology*, 53(4), 769–788. Available from: https://doi.org/10.1111/j.1365-3091.2006.00792.x

Brooke, B.P., Pietsch, T.J., Olley, J.M., Sloss, C.R. & Cox, M.E. (2015) A preliminary OSL chronology for coastal dunes on Moreton island, Queensland, Australia – marginal deposits of a large-scale quaternary shelf sediment system. *Cont Shelf Res*, 105, 79–94. Available from: https://doi.org/10.1016/j.csr.2015.06.002

Brooke, B., Ryan, D., Pietsch, T., Olley, J., Douglas, G., Packett, R., et al. (2008) Influence of climate fluctuations and changes in catchment land use on Late Holocene and modern beach-ridge sedimentation on a tropical macrotidal coast: Keppel Bay, Queensland, Australia. *Marine Geology*, 251(3), 195–208. Available from: https://doi.org/10.1016/j.margeo.2008.02.013

Bruun, P. (1962) Sea-level rise as a cause of shore erosion. *Journal of the Waterways and Harbors Division*, 88(1), 117–130. Available from: https://doi.org/10.1061/JWHEAU.0000252

Casella, E., Drechsel, J., Winter, C., Benninghoff, M. & Rovere, A. (2020) Accuracy of sand beach topography surveying by drones and photogrammetry. *Geo-Mar Lett*, 40(2), 255–268. Available from: https://doi.org/10.1007/s00367-020-00638-8

Choowong, M., Phantuwongraj, S., Charoentitirat, T., Chutakositkanon, V., Yumuang, S. & Charusiri, P. (2009) Beach recovery after 2004 Indian Ocean tsunami from Phang-nga, Thailand. *Geomorphology*, 104(3), 134–142. Available from: https://doi.org/10.1016/j.geomorph.2008.08.007

Cisternas, M., Mizobe, C., Wesson, R., Ely, L., Muñoz, A., Dura, T., Valdebenito, G., & Melnick, D. (2017). *Beach ridges, buried erosional scarps and overhanging soils evidence recurring past co-seismic subsidence midway along the area of the Giant 1960 Chile earthquake*. Geological Society of America Abstracts with Programs. Vol. 49, No. 6. Seattle, WA, USA. https://doi.org/10.1130/abs/2017AM-302380

Darwin, C. (1839) *Narrative of the surveying voyages of his Majesty's ships adventure and beagle, between the years 1826 and 1836: journal and remarks, 1832–1836 Vol. 3*. Henry Colburn, London.

Darwin, C. (1846) *Geological observations on South America. Being the third part of the geology of the voyage of the beagle, under the command of Capt. Fitzroy, R.N. during the years 1832 to 1836*. Smith Elder and Co, London.

Davies, J.L. (1974) The coastal sediment compartment. *Australian Geographical Studies*, 12(2), 139–151. Available from: https://doi.org/10.1111/j.1467-8470.1974.tb00270.x

Dickson, M.E., Omidiji, J., Litchfield, N.J., Norton, K.P., Matsumoto, H., Krier-Mariani, R.L., et al. (2022) Observations of the incipient and penultimate stages of Holocene marine terrace development. *Earth Surf Process Landf*, 47(13), 3019–3032. Available from: https://doi.org/10.1002/esp.5440

Egbert, G.D. & Erofeeva, S.Y. (2002) Efficient inverse modeling of Barotropic Ocean tides. *J Atmos Oceanic Tech*, 19(2), 183–204. Available from: https://doi.org/10.1175/1520-0426(2002)019<0183:EIMOBO>2.0.CO;2

FitzRoy, R. (1839) *Narrative of the surveying voyages of his Majesty's ships adventure and beagle, between the years 1826 and 1836, proceedings of the second expedition, 1831–1836 Vol. 2*. Henry Colburn, London.

Goff, J. & Sugawara, D. (2014) Seismic-driving of sand beach ridge formation in northern Honshu, Japan? *Mar Geol*, 358, 138–149. Available from: https://doi.org/10.1016/j.margeo.2014.04.005

Gonçalves, J.A. & Henriques, R. (2015) UAV photogrammetry for topographic monitoring of coastal areas. *ISPRS Journal of Photogrammetry and Remote Sensing*, 104, 101–111. Available from: https://doi.org/10.1016/j.isprsjprs.2015.02.009

Harley, M.D., Turner, I.L., Kinsela, M.A., Middleton, J.H., Mumford, P.J., Splinter, K.D., et al. (2017) Extreme coastal erosion enhanced by anomalous extratropical storm wave direction. *Sci Rep*, 7(1), 6033. Available from: https://doi.org/10.1038/s41598-017-05792-1

Hesp, P.A. (2013) Conceptual models of the evolution of transgressive dune field systems. *Geomorphology*, 199, 138–149. Available from: https://doi.org/10.1016/j.geomorph.2013.05.014

Hesp, P.A., DaSilva, M., Miot da Silva, G., Bruce, D. & Keane, R. (2022) Review and direct evidence of transgressive aeolian sand sheet and dunefield initiation. *Earth Surf Process Landf*, 47(11), 2660-2675. Available from: https://doi.org/10.1002/esp.5400

Jaramillo, E., Dugan, J.E., Hubbard, D.M., Melnick, D., Manzano, M., Duarte, C., et al. (2012) Ecological implications of extreme events: footprints of the 2010 earthquake along the Chilean coast. *PLoS ONE*, 7(5), e35348. Available from: https://doi.org/10.1371/journal.pone.0035348

Jara-Muñoz, J. & Melnick, D. (2015) Unraveling Sea-level variations and tectonic uplift in wave-built marine terraces, Santa María Island, Chile. *Quatern Res*, 83(1), 216–228. Available from: https://doi.org/10.1016/j.yqres.2014.10.002

Jara-Muñoz, J., Melnick, D., Zambrano, P., Rietbrock, A., González, J., Argandoña, B., et al. (2017) Quantifying offshore fore-arc deformation and splay-fault slip using drowned Pleistocene shorelines, Arauco Bay, Chile. *J Geophys Res Solid Earth*, 122(6), 4529–4558. Available from: https://doi.org/10.1002/2016JB013339

King, P.P. (1839) *Narrative of the surveying voyages of his Majesty's ships adventure and beagle: between the years 1826 and 1836*, Vol. 3. Henry Colburn, London.

King, C.A.M. & Williams, W.W. (1949) The formation and movement of sand bars by wave action. *The Geographical Journal*, 113, 70–85. Available from: https://doi.org/10.2307/1788907

Kölbl-Ebert, M. (1999) Observing orogeny — Maria Graham's account of the earthquake in Chile in 1822. *International Union of Geological Sciences*, 22(1), 36–40. Available from: https://doi.org/10.18814/epiiugs/1999/v22i1/006

Liew, S.C., Gupta, A., Wong, P.P. & Kwoh, L.K. (2010) Recovery from a large tsunami mapped over time: the Aceh coast, Sumatra. *Geomorphology*, 114(4), 520–529. Available from: https://doi.org/10.1016/j.geomorph.2009.08.010

Luijendijk, A., Hagenaars, G., Ranasinghe, R., Baart, F., Donchyts, G. & Aarninkhof, S. (2018) The state of the World's beaches. *Sci Rep*, 8(1), 6641. Available from: https://doi.org/10.1038/s41598-018-24630-6

MacDonald, K.E., Hart, D.E. & Pitman, S.J. (2021) Geomorphic responses of uplifted mixed sand and gravel beaches: combining short-term observations from Kaikōura, New Zealand with longer-term evidence. *New Zealand Journal of Geology and Geophysics*, 1-16, 1–16. Available from: https://doi.org/10.1080/00288306.2021.1994425

Martínez, C., Grez, P.W., Martín, R.A., Acuña, C.E., Torres, I. & Contreras-López, M. (2021) Coastal erosion in sandy beaches along a tectonically active coast: the Chile study case. *Progress in Physical Geography: Earth and Environment*, 46(2), 250–271. Available from: https://doi.org/10.1177/03091333211057194

Martínez, C., Rojas, D., Quezada, M., Quezada, J. & Oliva, R. (2015) Post-earthquake coastal evolution and recovery of an embayed beach in Central-Southern Chile. *Geomorphology*, 250, 321–333. Available from: https://doi.org/10.1016/j.geomorph.2015.09.015

Masselink, G., Castelle, B., Scott, T., Dodet, G., Suanez, S., Jackson, D., et al. (2016) Extreme wave activity during 2013/2014 winter and morphological impacts along the Atlantic coast of Europe. *Geophys Res Lett*, 43(5), 2135–2143. Available from: https://doi.org/10.1002/2015GL067492

McSaveney, M.J., Graham, I.J., Begg, J.G., Beu, A.G., Hull, A.G., Kim, K., et al. (2006) Late Holocene uplift of beach ridges at Turakirae head, South Wellington coast, New Zealand. *New Zealand Journal of Geology and Geophysics*, 49(3), 337–358. Available from: https://doi.org/10.1080/00288306.2006.9515172

Meilianda, E., Dohmen-Janssen, C.M., Maathuis, B.H.P., Hulscher, S.J.M. H. & Mulder, J.P.M. (2010) Short-term morphological responses and developments of Banda Aceh coast, Sumatra Island, Indonesia after the tsunami on 26 December 2004. *Mar Geol*, 275(1), 96–109. Available from: https://doi.org/10.1016/j.margeo.2010.04.012

Melnick, D., Bookhagen, B., Echtler, H.P. & Strecker, M.R. (2006) Coastal deformation and great subduction earthquakes, Isla Santa María, Chile (37°S). *GSA Bulletin*, 118(11–12), 1463–1480. Available from: https://doi.org/10.1130/B25865.1

Melnick, D., Cisternas, M., Moreno, M. & Norambuena, R. (2012) Estimating coseismic coastal uplift with an intertidal mussel: calibration for the 2010 Maule Chile earthquake (mw = 8.8). *Quaternary Science Reviews*, 42, 29–42. Available from: https://doi.org/10.1016/j.quascirev.2012.03.012

Melnick, D., Moreno, M., Motagh, M., Cisternas, M. & Wesson, R.L. (2012) Splay fault slip during the mw 8.8 2010 Maule Chile earthquake: REPLY. *Geology*, 41(12), e310–e310. Available from: https://doi.org/10.1130/G34825Y.1

Melnick, D., Moreno, M., Quinteros, J., Baez, J.C., Deng, Z., Li, S., et al. (2017) The super-interseismic phase of the megathrust earthquake cycle in Chile. *Geophys Res Lett*, 44(2), 784-791. Available from: https://doi.org/10.1002/2016GL071845

Mentaschi, L., Vousdoukas, M.I., Pekel, J.-F., Voukouvalas, E. & Feyen, L. (2018) Global long-term observations of coastal erosion and accretion. *Sci Rep*, 8(1), 12876. Available from: https://doi.org/10.1038/s41598-018-30904-w

Meyers, R.A., Smith, D.G., Jol, H.M. & Peterson, C.D. (1996) Evidence for eight great earthquake-subsidence events detected with ground-penetrating radar, Willapa barrier, Washington. *Geology*, 24(2),

99–102. Available from: https://doi.org/10.1130/0091-7613(1996)024<0099:EFEGES>2.3.CO;2

Monecke, K., Meilianda, E., Walstra, D.-J., Hill, E.M., McAdoo, B.G., Qiu, Q., et al. (2017) Postseismic coastal development in Aceh, Indonesia - field observations and numerical modeling. *Mar Geol*, 392, 94–104. Available from: https://doi.org/10.1016/j.margeo.2017.07.012

Monecke, K., Templeton, C.K., Finger, W., Houston, B., Luthi, S., McAdoo, B.G., et al. (2015) Beach ridge patterns in West Aceh, Indonesia, and their response to large earthquakes along the northern Sunda trench. *Quaternary Science Reviews*, 113, 159–170. Available from: https://doi.org/10.1016/j.quascirev.2014.10.014

Moore, L.J. (2000) Shoreline mapping techniques. *J Coast Res*, 16(1), 111–124. http://www.jstor.org/stable/4300016

Moreno, M., Melnick, D., Rosenau, M., Baez, J., Klotz, J., Oncken, O., et al. (2012) Toward understanding tectonic control on the mw 8.8 2010 Maule Chile earthquake. *Earth Planet Sci Lett*, 321-322, 152–165. Available from: https://doi.org/10.1016/j.epsl.2012.01.006

Moseley, M.E., Wagner, D. & Richardson, J.B.I.I.I. (1991) Chapter 10. Space shuttle imagery of recent catastrophic change along the arid Andeancoast. In: Johnson, L.L. (Ed.), *Paleoshorelines and Prehistory: An Investigation of Method*. CRC Press, Boca Raton, FL, 215–235.

Ojeda, J., Ruiz, S., del Campo, F. & Carvajal, M. (2020) The 21 may 1960 mw 8.1 Concepción earthquake: a deep megathrust foreshock that started the 1960 central-south Chilean seismic sequence. *Seismol Res Lett*, 91(3), 1617–1627. Available from: https://doi.org/10.1785/0220190143

Pajak, M.J. & Leatherman, S. (2002) The high water line as shoreline indicator. *J Coast Res*, 18(2), 329–337. http://www.jstor.org/stable/4299078

Peterson, C.D., Doyle, D.L. & Barnett, E.T. (2000) Coastal flooding and beach retreat from coseismic subsidence in the Central Cascadia margin, USA. *Environ Eng Geosci*, 6(3), 255–269. Available from: https://doi.org/10.2113/gseegeosci.6.3.255

Peterson, C.D., Jol, H.M., Vanderburgh, S., Phipps, J.B., Percy, D. & Gelfenbaum, G. (2010) Dating of late Holocene beach shoreline positions by regional correlation of coseismic retreat events in the Columbia River littoral cell, USA. *Mar Geol*, 273(1), 44–61. Available from: https://doi.org/10.1016/j.margeo.2010.02.003

Pinegina, T.K., Bourgeois, J., Bazanova, L.I., Zelenin, E.A., Krasheninnikov, S.P. & Portnyagin, M.V. (2020) Coseismic coastal subsidence associated with unusually wide rupture of prehistoric earthquakes on the Kamchatka subduction zone: a record in buried erosional scarps and tsunami deposits. *Quaternary Science Reviews*, 233, 106171. Available from: https://doi.org/10.1016/j.quascirev.2020.106171

Pinegina, T.K., Bourgeois, J., Kravchunovskaya, E.A., Lander, A.V., Arcos, M.E.M., Pedoja, K., et al. (2013) A nexus of plate interaction: vertical deformation of Holocene wave-built terraces on the Kamchatsky peninsula (Kamchatka, Russia). *GSA Bulletin*, 125(9–10), 1554–1568. Available from: https://doi.org/10.1130/B30793.1

Plafker, G. (1972) Alaskan earthquake of 1964 and Chilean earthquake of 1960: implications for arc tectonics. *Journal of Geophysical Research (1896–1977)*, 77(5), 901–925. Available from: https://doi.org/10.1029/JB077i005p00901

Plafker, G. & Savage, J.C. (1970) Mechanism of the Chilean earthquakes of may 21 and 22, 1960. *GSA Bulletin*, 81(4), 1001–1030. Available from: https://doi.org/10.1130/0016-7606(1970)81[1001:MOTCEO]2.0.CO;2

Pucino, N., Kennedy, D.M., Carvalho, R.C., Allan, B. & Ierodiaconou, D. (2021) Citizen science for monitoring seasonal-scale beach erosion and behaviour with aerial drones. *Sci Rep*, 11(1), 3935. Available from: https://doi.org/10.1038/s41598-021-83477-6

Rabassa, J. & Clapperton, C.M. (1990) Quaternary glaciations of the southern Andes. *Quaternary Science Reviews*, 9(2), 153–174. Available from: https://doi.org/10.1016/0277-3791(90)90016-4

Rajendran, C.P., Rajendran, K., Anu, R., Earnest, A., Machado, T., Mohan, P.M., et al. (2007) Crustal deformation and seismic history associated with the 2004 Indian Ocean earthquake: a perspective

from the Andaman–Nicobar Islands. *Bull Seismol Soc am*, 97(1A), S174–S191. Available from: https://doi.org/10.1785/0120050630

Ranasinghe, R. (2016) Assessing climate change impacts on open sandy coasts: a review. *Earth-Science Reviews*, 160, 320–332. Available from: https://doi.org/10.1016/j.earscirev.2016.07.011

Saha, S., Moorthi, S., Pan, H.-L., Wu, X., Wang, J., Nadiga, S., et al. (2010) The NCEP climate forecast system reanalysis. *Bull am Meteorol Soc*, 91(8), 1015–1058. Available from: https://doi.org/10.1175/2010BAMS3001.1

Sallenger, A.H.J. (2000) Storm impact scale for Barrier Islands. *J Coast Res*, 16(3), 890–895. http://www.jstor.org/stable/4300099

Smith, J. M. (2001). *Modeling nearshore wave transformation with STWAVE*. U.S. Army Engineer Research and Development Center, Vicksburg, MS, USA.

Stockdon, H.F., Holman, R.A., Howd, P.A. & Sallenger, A.H. (2006) Empirical parameterization of setup, swash, and runup. *Coastal Engineering*, 53(7), 573–588. Available from: https://doi.org/10.1016/j.coastaleng.2005.12.005

Tappin, D.R., Evans, H.M., Jordan, C.J., Richmond, B., Sugawara, D. & Goto, K. (2012) Coastal changes in the Sendai area from the impact of the 2011 Tōhoku-oki tsunami: interpretations of time series satellite images, helicopter-borne video footage and field observations. *Sedimentary Geology*, 282, 151–174. Available from: https://doi.org/10.1016/j.sedgeo.2012.09.011

Thieler, E. R., Himmelstoss, E. A., Zichichi, J. L., & Ergul, A. (2009). *The digital shoreline analysis system (DSAS) version 4.0 - an ArcGIS extension for calculating shoreline change [report](2008-1278)*. Open-File Report, Issue.U. S. Geological Survey,Reston, VA, USA. http://pubs.er.usgs.gov/publication/ofr20081278

Tolman, H., Accensi, M., Alves, J.-H., Ardhuin, F., Bidlot, J., Booij, N., Bennis, A.-C., Campbell, T., Chalikov, D., Filipot, J.-F., Foreman, M., Janssen, P., Leckler, F., Li, J.-G., Chawla, A., Lind, K., Orzech, M., Padilla-Hernandez, R., Rogers, E., & Zieger, S. (2014). *User manual and system documentation of WAVEWATCH III version 4.18*. NOAA/NWS/NCEP/MMAB, Technical Report, 311p. College Park, Maryland.

Tzanis, A. (2010). *MATGPR release 2 : a freeware MATLAB ® package for the analysis & interpretation of common & single offset GPR data*. FastTimes, 15 (1), 17–43.

Vargas, G., Farias, M., Carretier, S., Tassara, A., Baize, S. & Melnick, D. (2011) Coastal uplift and tsunami effects associated to the 2010 M(w)8.8 Maule earthquake in Central Chile. *Andean Geology*, 38(1), 219–238. https://publishup.uni-potsdam.de/frontdoor/index/index/docId/37132

Vos, K., Harley, M.D., Splinter, K.D., Simmons, J.A. & Turner, I.L. (2019) Sub-annual to multi-decadal shoreline variability from publicly available satellite imagery. *Coastal Engineering*, 150, 160–174. Available from: https://doi.org/10.1016/j.coastaleng.2019.04.004

Vos, K., Splinter, K.D., Harley, M.D., Simmons, J.A. & Turner, I.L. (2019) CoastSat: a Google earth engine-enabled python toolkit to extract shorelines from publicly available satellite imagery. *Environ Model Software*, 122, 104528. Available from: https://doi.org/10.1016/j.envsoft.2019.104528

Wang, B., Shi, W. & Liu, E. (2015) Robust methods for assessing the accuracy of linear interpolated DEM. *International Journal of Applied Earth Observation and Geoinformation*, 34, 198–206. Available from: https://doi.org/10.1016/j.jag.2014.08.012

Wells, A. & Goff, J. (2006) Coastal dune ridge systems as chronological markers of palaeoseismic activity: a 650-yr record from southwest New Zealand. *The Holocene*, 16(4), 543–550. https://doi.org/10.1191/0959683606hl949rp

Wesson, R. (2017) *Darwin's first theory: exploring Darwin's quest for a theory of earth*. Pegasus Books, New York, USA.

Wesson, R.L., Melnick, D., Cisternas, M., Moreno, M. & Ely, L.L. (2015) Vertical deformation through a complete seismic cycle at Isla Santa María, Chile. *Nature Geoscience*, 8(7), 547–551. Available from: https://doi.org/10.1038/ngeo2468

Winckler, P., Contreras-López, M., Campos-Caba, R., Beyá, J.F. & Molina, M. (2017) El temporal del 8 de agosto de 2015 en las

regiones de Valparaíso y Coquimbo, Chile Central. *Lat am J Aquat Res*, 45(4), 622–648. http://www.scielo.cl/scielo.php?script=sci_arttext&pid=S0718-560X2017000400622&nrm=iso. Available from: https://doi.org/10.3856/vol45-issue4-fulltext-1

SUPPORTING INFORMATION

Additional supporting information can be found online in the Supporting Information section at the end of this article.